OBSERVATION AND MODELING OF HIGH-n IRON L-SHELL LINES FROM INTERMEDIATE ION STAGES

B. J. WARGELIN,[1,2] P. BEIERSDORFER,[3] D. A. LIEDAHL,[3] S. M. KAHN,[1,4] AND S. VON GOELER[5]

ABSTRACT

The spectra of highly ionized iron species between 7 and 9 Å have been studied using data obtained at the Princeton Large Torus tokamak under plasma conditions similar to those present in solar and stellar flares. The wavelengths of many iron lines are measured with very high accuracy ($\lambda/\Delta\lambda$ up to 4×10^4), along with several other lines in species such as He-like Al XII and Mg XI. Theoretical spectra that predict both the wavelength and the intensity of Fe emission lines are compared with the observed spectra and are used to make accurate line identifications. Virtually all the observed iron lines are found to arise from $n = 4$, 5, and $6 \rightarrow 2$ transitions in Fe XXI–XXIV, and many lines are identified for the first time. Several transitions are shown to have diagnostic applications, and a detailed analysis of the density sensitivity of Fe XXII lines is presented.

Subject headings: atomic data — line: identification — Sun: X-rays, gamma rays — X-rays: general

1. INTRODUCTION

Emission lines arising from $n = 4 \rightarrow 2$ and $n = 5 \rightarrow 2$ transitions in highly ionized iron species such as Fe XXI–XXIV have been observed for many years in the X-ray spectra of solar flares (Doschek, Meekins, & Cowans 1972; Seely & Feldman 1986; McKenzie et al. 1985; Fawcett et al. 1987) and are expected to be seen in most classes of X-ray sources by next generation X-ray spectroscopy satellite missions such as the *Advanced X-Ray Astrophysics Facility* (*AXAF*) and the *X-Ray Multi-Mirror Mission* (*XMM*). Many of these lines are quite prominent, and several can be used to infer the physical parameters of the emitting gas, including electron density, temperature, charge-state distribution, and deviations from coronal ionization equilibrium.

Instrumental considerations also encourage the study of $4 \rightarrow 2$ and $5 \rightarrow 2$ transitions. Most of these lines fall between 7 and 9 Å, a range particularly well suited for study using stable and high-resolution diffraction crystals such as ammonium dihydrogen phosphate (ADP), with lattice spacing $2d = 10.648$ Å. In addition, the photon energy is above the low-energy cutoff below which most detectors' quantum efficiency rapidly declines because of photoabsorption in windows or surface layers. In particular, *AXAF*'s effective area, when using either grating/detector combination, peaks in just this energy range. Likewise, for astrophysical sources, photoabsorption by circumstellar and interstellar material is less problematic than it is at longer wavelengths. Finally, most $4 \rightarrow 2$ and $5 \rightarrow 2$ lines are well separated, requiring a resolving power of only a few hundred for effective application of diagnostic line-intensity ratios.

Clear illustrations of the importance of accurate atomic rate data (for Fe L-shell emission in particular) in analyzing astrophysical X-ray spectra were recently provided by the *Advanced Satellite for Cosmology and Astrophysics* (*ASCA*). Several observations showed that existing plasma-emission models, or rather, the emission rates they incorporated, could not provide adequate fits to the spectral data for any set of physically reasonable plasma parameters (Drake et al. 1994; Fabian et al. 1994; White et al. 1994). Indeed, subsequent atomic modeling results showed that the intensity of the $3 \rightarrow 2$ line complex relative to that of the $4 \rightarrow 2$ blend had been underestimated by a factor of approximately 2 (Liedahl, Osterheld, & Goldstein 1995). These errors were discovered during an analysis of astrophysical spectra with a resolving power of only 20 (near 10 Å); the high-resolution spectral data expected from future missions will provide even greater challenges for spectral modeling codes.

Using theoretical atomic models (Doschek et al. 1972; Bromage et al. 1978; Fawcett et al. 1987) and comparisons with laser plasma spectra (Boiko, Faenov, & Pikuz 1978; Fawcett & Ridgeley 1979), many of the transitions seen in solar spectra between 7 and 9 Å have been identified. Several important features remain unidentified, however, and very little quantitative work has been done on the diagnostic uses of iron lines in this wavelength band (see Mason & Storey 1980). With adequate knowledge of relevant atomic parameters, however, plasma diagnostics based on $4 \rightarrow 2$ and $5 \rightarrow 2$ lines sometimes can be more useful than those relying on the more familiar $3 \rightarrow 2$ transitions.

In this paper we present spectra of highly ionized iron between 7.1 and 9.0 Å obtained at the Princeton Large Torus (PLT) tokamak, which has temperatures and densities similar to those in solar and stellar plasmas. We compare these high-resolution spectra with results from a detailed atomic model of Fe ions, which allows us to make several new line identifications and to develop density diagnostics for astrophysical use. The wavelengths of many lines are measured with unprecedented precision, and a few previously published identifications are corrected. We also identify and accurately measure the wavelengths of several

[1] Department of Physics and Space Sciences Laboratory, University of California, Berkeley, CA 94720.

[2] Present address: Harvard-Smithsonian Center for Astrophysics, 60 Garden Street, Cambridge, MA 02138.

[3] Lawrence Livermore National Laboratory, 7000 East Avenue, Livermore, CA 94550.

[4] Present address: Department of Physics, Columbia University, 538 West 120th Street, New York, NY 10027.

[5] Princeton Plasma Physics Laboratory, Princeton University, Princeton, NJ 08543.

lines from other common elements that occur in this wavelength region.

In § 2 we discuss plasma conditions in the PLT tokamak, the spectrometer used, and our analysis and calibration procedure. In § 3 we describe the HULLAC computational suite and the assumptions made in our calculations. In § 4 we present our observations and line identifications, and in § 5 we discuss line-intensity ratios that can be used as diagnostics.

2. DATA COLLECTION

2.1. The Princeton Large Torus Tokamak

Tokamaks, designed for fusion research, have provided abundant information about the physics of highly charged ions (von Goeler et al. 1981; Hinnov 1982; Peacock, Stamp, & Silver 1984; Beiersdorfer et al. 1989). Virtually all existing tokamaks have stainless steel containment vessels, so there is always some background emission arising from highly ionized iron, as well as from smaller amounts of chromium, nickel, and other metals that are sputtered from the chamber walls or limiter plate. Indeed, early tokamaks were unable to attain their expected plasma temperatures because so much energy was lost via radiation from ambient iron ions. Subsequent tokamaks have been designed to minimize sputtering from interior surfaces and often use coatings of low-Z elements such as Be, B, and C so that emission from sputtered ions will be at lower power and photon energies.

Tokamaks have plasma conditions similar to those found in stellar coronae, particularly flares, which have typical densities of 10^{11}–10^{13} cm^{-3} and temperatures up to a few times 10^7 K. As a result, spectra from a given element are similar, and results from laboratory observations can often be applied directly to astrophysical sources. Previous laboratory identifications of $4 \rightarrow 2$ and $5 \rightarrow 2$ transitions in Fe ions have made extensive and effective use of laser plasmas (Boiko et al. 1978; Fawcett & Ridgeley 1979), which typically have densities of order 10^{20} cm^{-3}. At such high densities, however, opacity and satellite broadening effects are often significant, and metastable levels may be collisionally excited to higher levels, which results in radiative transitions that rarely occur in astrophysical X-ray sources. Another difference is that tokamak plasmas are much larger than laser plasmas, which allows the effective use of curved crystal spectrometers that can be used to map out detailed dispersion curves and provide extremely accurate wavelength measurements. Precise line positions make it easier to identify transitions when comparing observations with theoretical predictions, and they permit more reliable line-intensity measurements when lines are partially blended.

The experiments described here were performed on the PLT (Hosea, Goldston, & Colestock 1985), a medium-size tokamak with major and minor radii of 134 and 40 cm, respectively. Typical central electron temperatures when using ohmic heating are 0.8–3.0 keV [corresponding to (1–3.5) × 10^7 K], with temperatures falling toward the chamber walls following a roughly Gaussian profile. Line-of-sight–averaged electron densities are in the range of (0.2–10.0) × 10^{13} cm^{-3}, with a typical value of a few times 10^{13}. Densities are highest in the center of the plasma and have a somewhat flattened parabolic spatial profile. A typical plasma discharge, or "shot," lasts about 1 s, and trace amounts of other elements can be injected into the hydrogen plasma during each shot to study emission spectra, either for wavelength calibration or for diagnosis of plasma parameters. Temperature and density can also be measured independently using Thomson scattering and Michelson interferometry, respectively.

2.2. Spectrometer

We used a high-resolution vacuum spectrometer with a Bragg crystal and Johann geometry, as described by Beiersdorfer et al. (1989), to record the X-ray spectra presented here. A curved ADP crystal (57.3 cm radius of curvature) focused X-rays from the plasma onto a position-sensitive detector according to the Bragg equation, $\lambda = 2d \sin \theta$, where d is the crystal plane spacing ($2d = 10.648$ Å for ADP) and θ is the Bragg angle of diffraction. In this geometry, diffracted X-rays having different wavelengths originate from different regions of the plasma.

The first element of our detector was a flat "chevron" configuration microchannel plate, which was coated with approximately 3000 Å of CsI to increase X-ray–to–electron conversion efficiency. Secondary electrons were proximity-focused onto a fiber-optic surface coated with about 8 μm of P-20 phosphor. Light signals then traveled down two fiber-optic tapers to two 1024 channel Reticon photodiode arrays. During each plasma discharge, the array was read out every 4 ms over a period of 192 ms for a total of 48 spectra.

Ideally, the detector face would be curved to match the Rowland circle, but since our detector was relatively small, focusing errors did not significantly degrade resolution; the crystal could also be slightly pivoted on its axis, and diffracted lines could still be adequately focused on the microchannel plate face. To extend the wavelength coverage of the spectrometer further (the bandpass for a single crystal position was typically 1 Å), the entire spectrometer was tilted, which required careful repositioning of the detector along the Rowland circle defined by the crystal position and orientation.

Our data were obtained using three detector positions, covering three partially overlapping wavelength regions that we refer to as short-, medium-, and long-wavelength ranges. Each of these data sets was further subdivided into two halves by the two-piece fiber-optic taper. The result was six sets of data, each of which required its own wavelength calibration. Because of the nonlinear dispersion characteristics of the spectrometer and slight spatial distortions in the microchannel plate and optical tapers, it was necessary to map out dispersion curves actively in order to obtain the desired wavelength measurement accuracy.

2.3. Calibration

To calibrate the wavelengths of observed lines, we injected very small amounts of sodium or magnesium into the plasma by using the laser "blow-off" method (Marmar, Cecchi, & Cohen 1975). Approximately 15 ms after injection and 35 ms after the start of data acquisition, the injected ions began emitting prominent K series ($1s^2$ $^1S_0$–$1s$ np $^1P_1$) and Lyman series lines.[6] Figure 1 shows some typical spectra obtained before and during calibration line emission.

Sodium and magnesium were chosen as calibrators because a large number of their K and Lyman emission

---

[6] We use the "K" label only for He-like emission lines, in order to distinguish them from the H-like Lyman lines.
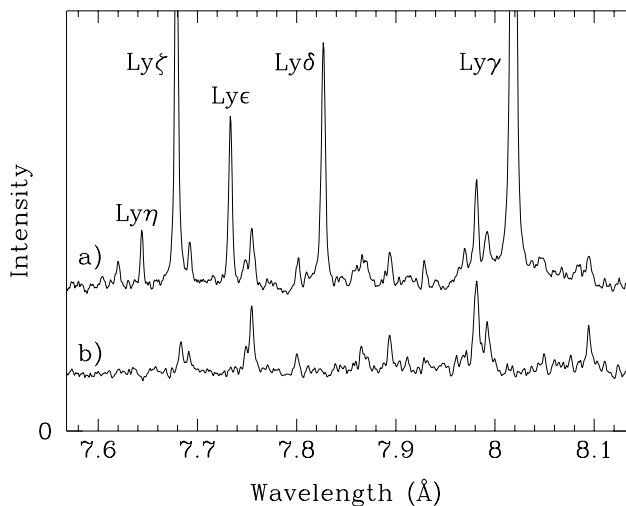
FIG. 1.—Example spectra taken (a) during and (b) before calibration line emission. Each spectrum was collected over a period of 28 ms. The calibration lines are from the Lyman series of hydrogenic Na XI. (The intensity of Lyζ is enhanced by charge-exchange recombination of bare Na XII with trace amounts of neutral hydrogen.) Background emission from Fe ions is present in both spectra, along with a few emission lines from residual Al and Se.

lines fall within the 7–9 Å range under study, and theoretical calculations of their wavelengths are very accurate. A list of the reference lines used is found in Table 1, along with the estimated uncertainty of each line's wavelength. We used the results of Garcia & Mack (1965) for the H-like lines. Their calculations include the weighted contributions of all $n \rightarrow 1$ components (not just the $^2P_{3/2}$ and $^2P_{1/2}$ terms) and are accurate to better than 0.0001 Å. For Mg Lyα, which has an asymmetric line profile (Lyα$_1$ and Lyα$_2$ at 8.4192 and 8.4246 Å are not resolved in our data), we allowed an uncertainty of 0.0003 Å to account for any errors introduced by our assumption of a 2:1 intensity ratio of the two Lyα components. For the He-like lines we used the predictions of U. I. Safronova (1986, private communication), which we believe are more accurate than the wavelengths listed in Kelly (1987, pp. 186, 215). The uncertainty we assumed for each line is generally the differ-

TABLE 1
WAVELENGTH CALIBRATION LINES

Ion	Transition	Wavelength (Å)	References
Mg^{10+}	Kε	7.2247 ± 0.0003	1
Mg^{10+}	Kδ	7.3103 ± 0.0002	1
Mg^{10+}	Kγ	7.4731 ± 0.0002	1
Na^{10+}	Lyη	7.63936 ± 0.0001	2
Na^{10+}	Lyζ	7.67662 ± 0.0001	2
Na^{10+}	Lyε	7.73477 ± 0.0001	2
Na^{10+}	Lyδ	7.83318 ± 0.0001	2
Mg^{10+}	Kβ	7.8503 ± 0.0002	3
Na^{10+}	Lyγ	8.02107 ± 0.0001	2
Mg^{11+}	Lyα	8.42100 ± 0.0003	2
Na^{10+}	Lyβ	8.45950 ± 0.0001	2
Na^{9+}	Kε	8.6863 ± 0.0004	1
Na^{9+}	Kδ	8.7885 ± 0.0003	1
Na^{9+}	Kγ	8.9830 ± 0.0002	1

REFERENCES.—(1) U. T. Safronova, private communication, (2) Garcia & Mack 1965; (3) this work, measured using nearby Na^{10+} Lyman series lines.

ence between Safronova's and Kelly's values and makes ample allowance for the fact that the He-like calculations are for only the $1s$ np $^1P_1 \rightarrow$ $^1S_0$ transitions. Weak transitions from other excited levels (such as $1s$ np $^3P_1$) will slightly shift the centroid of the blended line, but this effect is negligible for all the He-like calibration lines appearing in our spectra except for Mg Kβ. In that case, the effective wavelength of the Mg Kβ blend was itself calibrated using nearby Na Lyman lines, which provided a net wavelength accuracy of ±0.0002 Å.

The intrinsic resolving power of the spectrometer when perfectly focused was estimated to be 3500 (Beiersdorfer et al. 1989). The FWHM of the Doppler-broadened lines was measured to be as small as 0.003 Å (about six detector channels), corresponding to $\lambda/\Delta\lambda \approx 2500$. Since the center of a strong line can be measured to a small fraction of its FWHM, the wavelength differences between lines can be determined with high precision. In most cases, however, it is impossible to exploit this potential precision fully in wavelength measurements because the exact dispersion curve is not well determined.

As mentioned previously, however, the crystal in our spectrometer could rotate over a small range without significantly degrading the spectral resolution. Such rotations move the diffracted spectrum across the face of the detector, but the angular separations of line pairs (determined by the Bragg diffraction condition) remain the same even though their physical separation on the detector changes. We utilized this fact to map out a very precise dispersion curve for each of the six data sets (two detector halves for each of three detector positions) by observing how the channel spacing between pairs of calibration lines changed as those lines moved across the detector. Defining κ as $d\theta/dN$, where θ is the Bragg angle and N is the detector channel number, the angular separation $\Delta\theta$ between any two lines is then

$$\Delta\theta = \theta_2 - \theta_1 = \int_{N_1}^{N_2} \kappa(N)dN , \qquad (1)$$

where θ_1 and N_1 are, respectively, the Bragg angle and detector channel number corresponding to the first line, and θ_2 and N_2 correspond to the second line.

Taking pairs of calibration lines with known detector positions (channel numbers) and wavelengths (Bragg angles), we can then determine $\kappa(N)$ by using linear least-squares methods to find the best polynomial fit. Once κ is known as a function of N, the wavelength of any line can be calculated based upon the wavelength and position of a single calibration line using the equation

$$\lambda_{\mathrm{unknown}} = 2 d \sin (\theta_{\mathrm{cal}} + \Delta\theta) , \qquad (2)$$

where

$$\Delta\theta = \int_{N_{\mathrm{cal}}}^{N_{\mathrm{unknown}}} \kappa(N)dN . \qquad (3)$$

We determined $\kappa(N)$ for each data set using calibration data that were statistically weighted according to the uncertainty in each line's fitted channel position (using Voigt profiles) and wavelength (see Table 1). Second-order polynomials gave acceptable fits to five of the calibration data sets, while the first half of the medium-wavelength data required a third-order fit. That data set was exceptionally well constrained by its numerous and strong Na Lyman

series lines and permitted the wavelengths of several Fe lines to be measured to 0.0002 or 0.0003 Å. Near the ends of our spectral coverage, wavelength calibration was somewhat less precise for several reasons: (1) spectral resolution was worse because the crystal was at nonoptimal angles; (2) calibration-line wavelengths were not as accurately known; (3) both calibration and Fe lines were generally weaker. It was also observed that the positions of the longest wavelength lines drifted slightly during the course of a shot, but this phenomenon was very repeatable, and we minimized its impact by comparing calibration and Fe-emission data taken from identical time groups. As a result, a calibration accuracy of 0.001 Å or better was maintained over the entire range studied.

3. CALCULATED SPECTRA

The model spectra were calculated using the HULLAC atomic physics package. For the problem at hand, HULLAC was used to calculate the atomic structure of the ions Fe XXI–XXIV, the radiative decay rates, and the rate coefficients for electron impact excitation. These atomic data were then used to calculate the distribution of level populations within each charge state according to the equations of statistical equilibrium, from which the line spectrum follows. Model spectra from Cr XXI–XXII were also calculated since those ions have some emission lines in the wavelength range under study.

The atomic structure and radiative rates are calculated ab initio using a relativistic, multiconfiguration, parametric-potential method in intermediate coupling (Klapisch et al. 1977). HULLAC was developed for optimum performance with highly charged high-Z ions, for which intermediate coupling using j-j basis states is most appropriate. In this paper, LS-coupling notation is used when such a term can be unambiguously assigned (as for all Li-like and Be-like states, and B-like states with a $2s^2$ core). For B-like transitions involving a $2s$ electron, and for all C-like transitions, j-j–coupling notation has been used, along with LS terms suggested by other authors for previously identified lines.

The models used in the calculations are given in Table 2. Radiative transitions include the multipoles $E1$, $E2$, $M1$, and $M2$. The collisional cross sections are calculated according to the quasi-relativistic distorted wave approximation (Bar-Shalom, Klapisch, & Oreg 1988). Collisional-rate coefficients γ (units of $cm^3 s^{-1}$) are found by averaging $v\sigma(v)$ over a Maxwellian velocity distribution. The rate coefficients for collisional excitation from all states within configurations $(2s2p)^k$ to all excited states $(2s2p)^{k-1}nl$ in the models are calculated, as well as the $2l \rightarrow 2l'$ intrashell excitations.

Coupling of excited states to levels in adjacent charge states through inner shell ionization, dielectronic recombination (DR), and radiative recombination is ignored for several reasons. K-shell ionization of Fe ions in their ground states produces no emission in the spectral band studied here. DR, on the other hand, contributes $\sim 10\%$ of the total line flux, varying with temperature and ion species (Liedahl et al. 1995). For plasma temperatures of interest here, DR involving excitation of an L-shell electron is most important. Each such recombination begins with a radiationless capture of the form $(2s2p)^k + e \rightarrow (2s2p)^{k-1}nln'l'$ (n, $n' \geq 3$), which may stabilize with the emission of an X-ray satellite line. The excited but bound state left by stabilization, $(2s2p)^knl$, cascades to the ground state, with the eventual emission of another X-ray.

Of the two X-rays produced as a consequence of DR, only the satellite is distinct from the line produced directly through electron impact excitation and can, in principle, be identified. The satellite spectrum is, however, composed of a large number of weak lines, and except for the possibility of detecting the long-wavelength shoulders (unresolved satellites) of resonance lines of the recombining ion, DR-driven lines in these ions are generally too weak to select out from spectra measured in tokamak experiments. Ignoring recombination therefore cannot lead to line misidentification because of satellite contamination. Likewise, intensity enhancement of nonsatellite lines produced through DR-initiated cascades is too small an effect to isolate.

Radiative recombination is even less important than DR in driving $4 \rightarrow 2$ and $5 \rightarrow 2$ line emission in these ions (under conditions near coronal equilibrium) because the generally small rates are dominated by capture into the $n = 2$ and $n = 3$ levels, bypassing the higher n levels. Charge transfer from neutral hydrogen, in contrast, preferentially populates high-n levels, roughly $n = 9$–11 for the Fe charge states of interest here. Since radiative decays tend to proceed to the lowest energy level allowed by selection rules, most of those high-n levels either decay directly to a ground level (e.g., $10s \rightarrow 2p$), or fall as far as they can to intermediate-n levels with $l = l_{max} = n - 1$ (e.g., $10h \rightarrow 5g$), which then decay via $\Delta n = \Delta l = 1$ steps along the so-called Yrast chain (e.g., $5g \rightarrow 4f \rightarrow 3d \rightarrow 2p$). Such transitions are not expected to contribute appreciably to our spectra, and charge exchange is therefore not considered in our modeling calculations.

As shown in Table 2, two C-like Fe models were used in the calculations. As indicated, the 676 level model does not include the $n = 3$ or $n = 4$ shells. These were omitted in the calculations of $5 \rightarrow 2$ and $6 \rightarrow 2$ Fe XXI spectra simply to keep the size of the models manageable. This introduces

TABLE 2
CHARACTERISTICS OF ATOMIC MODELS USED IN CALCULATING MODEL SPECTRA

Name	Isosequence	Number of Levels	n_{max}	l_{max}	Number of Radiative Rates	Number of Collisional Rates[a]
Fe XXI	C	1004	5	4	132959	18662
	C	676	6[b]	3	63370	12099
Fe XXII	B	735	6	4	74338	10341
Fe XXIII	Be	302	7	4	12034	2900
Fe XXIV	Li	42	7	4	330	118
Cr XXI	Be	166	7	4	12019	2911
Cr XXII	Li	42	7	4	331	118

[a] Each rate computed on a 6 point temperature grid.
[b] Model does not include levels with principal quantum numbers $n = 3$ or 4.

small errors in the branching ratios of radiative transitions from $n = 5$ and $n = 6$ excited states, but the resulting errors in relative line intensities are also small and have no bearing on the results presented here.

4. OBSERVED SPECTRA AND LINE IDENTIFICATIONS

Some 60 shots, each with 48 time-binned spectra, were scanned for prominent features, and approximately 50 lines of high statistical significance and reproducibility were discerned, not counting the Na and Mg calibration lines. A composite spectrum is shown in Figure 2 with each feature labeled (see figure legend for labeling convention). Well over 30 Fe lines were identified, along with 10 lines from other elements, including Li-like Cr XXII.

The composite spectrum combines spectra collected using eight different detector-position or crystal-angle settings, which were chosen based on (1) high signal-to-noise ratio, (2) high resolution, and (3) exclusion of lines from elements other than Fe and Cr. In a few cases, it was impossible to avoid inclusion of some weak calibration lines below 7.5 Å, as well as a few lines from Al and Se. Those lines were excised from the composite spectrum (and labeled in parentheses) to facilitate comparison with the model spectrum, which includes emission from only Fe and Cr ions.

The component spectra were joined at 7.505, 7.814, 7.881, 7.958, 8.006, 8.106, 8.352, 8.413, 8.453, 8.498, 8.566, 8.851, and 8.943 Å, and their relative amplitudes and continuum levels were adjusted so that overlapping lines had approximately equal strength. As mentioned in § 2.2, within individual spectra focused X-rays of different wavelengths arise from different regions of the tokamak plasma, i.e., regions that have different temperatures, densities, and plasma column depths. Thus it can be seen that lines near the two ends of the composite spectrum become increasingly weak, since the spectrometer was collecting X-rays emitted near the edges of the tokamak plasma. Indeed, below about 7.4 Å, only a low-temperature, short-column portion of the plasma can be observed, and no lines from highly ionized Fe are seen.

The theoretical spectra used to identify transitions in the observed data are also shown in Figure 2, with line widths set to 0.0063 Å FWHM (corresponding to $\lambda/\Delta\lambda = 1270$ at 8 Å). Two such spectra are shown; both are composed of the same lines with the same intensities, but one employs line wavelengths that have been slightly adjusted (as described later in this section) to agree more closely with the observed spectrum, while the other uses the directly computed, uncorrected wavelengths. This illustrates how slight differences in line wavelengths can alter the appearance of spectra.

As discussed in § 3, the theoretical model includes emission from Fe XXI–XXIV and Cr XXII. Because the observed spectrum has been assembled from several shots, each occurring under somewhat different circumstances and each line originating from a different part of the plasma, the relative emission measure of each ion included in the theoretical model was adjusted "by eye" to match the observed data as well as possible. For simplicity, we set a temperature of 1000 eV for all ions—the relative line strengths within a given charge state depend only weakly on temperature—and adjusted the relative ion abundances as follows: Fe XXIV, 1.00; Fe XXIII, 0.78; Fe XXII, 0.61; Fe XXI, 0.063; Cr XXII, 0.78. Emission from Cr XXI, although calculated,

was not included in the model spectrum because it was not observed in the data. As will be discussed in § 5, the spectra of B- and C-like Fe depend on electron density; the spectrum shown assumes a density of $10^{13.5}$ cm^{-3}. As can be seen, the resulting theoretical and observed spectra match very well, with generally excellent agreement in wavelengths and relative intensities.

In Table 3 we list our Fe-line identifications, along with a comprehensive compilation of previous theoretical and observational work on Fe spectra between 7 and 9 Å with wavelength accuracies of 1 or 2 mÅ. The wavelengths reported by McKenzie et al. (1985) are also included (following a slight correction) even though the accuracy they quote is only 3 mÅ. Although their solar observations are of high quality and resolution, the measured wavelengths of well-studied transitions in hydrogenic and helium-like ions for lines between approximately 7.2 and 8 Å are systematically 3 or 4 mÅ longer than the known values, which indicates a calibration error. We therefore reduced their measured wavelengths by 0.003 Å for lines shortward of 8 Å, which brings their results into excellent agreement with other measurements.

Since our emphasis is on astrophysical applications, Table 3 does not include lines that have been observed only in laser plasma spectra, since many of those lines arise from doubly excited states, which can only be excited in extremely high density environments (Bromage et al. 1978). Using the same inclusion criteria as those used for Table 3, Table 4 lists unidentified lines that are believed to come from Fe based on a priori knowledge of plasma constituents. Table 5 lists lines from elements other than Fe that were observed in our spectra, several of which are prominent in solar flare spectra and have important diagnostic applications.

Nearly all of our wavelength measurements are accurate to 1 mÅ. Two exceptions are included in Tables 3 and 4, with uncertainties of 0.003 Å or more: line E1 (at ~ 7.478 Å) because of blending with residual Mg Kγ emission, and line U4 (at ~ 9.009 Å) because it was at the very edge of our spectral coverage and resolution was poor. In those cases where a measurement is accurate to better than 1 mÅ, the uncertainty in the last digit (tenths of 1 mÅ) is indicated in parentheses. We are able to measure the wavelengths of 27 lines to better than 1 mÅ. Five of those lines have been previously measured to an accuracy of 0.0007 Å by Seely & Feldman (1985), and our agreement with their results is excellent.

No accuracy estimates are provided for the theoretically calculated wavelengths listed in Table 3, but agreement between our calculations and observed values is excellent for the Fe XXIV lines. Agreement among the Fe XXIII lines is equally good, except for the six lines arising from transitions to the $2s2p\ ^1P_1$ level (lines E11, E10, E5, E4, E2, and part of the E1 blend), each of which had observed wavelengths that were approximately 0.010 Å shorter than those predicted by theory. We are unable to explain this discrepancy, but note that if the calculated energy of the $2s2p\ ^1P_1$ level is decreased from 95.1 to 93.2 eV (above the $2s^2\ ^1S_0$ ground state), the wavelengths of all six lines are brought to within 0.001 Å of their respective observed values. It is interesting that the calculations of Fawcett et al. (1987) apparently have a similar error in the energy of the $2s2p\ ^1P_1$ level, but no other Fe XXIII levels.

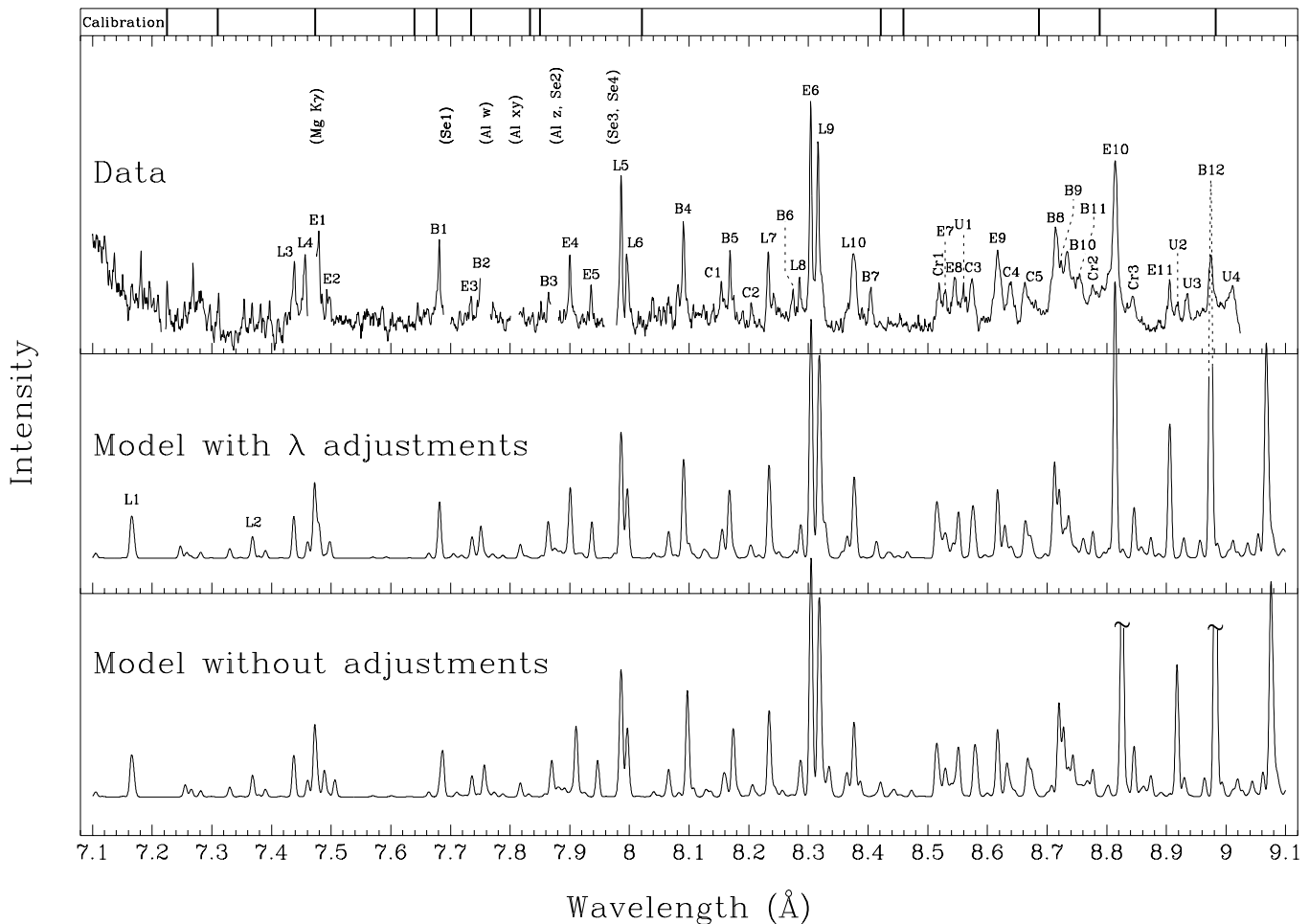For transitions in B-like Fe XXII, our calculated wave-

FIG. 2.—Observed and model spectra. The observed spectrum is a composite; the different sections have been adjusted in amplitude to maintain reasonably consistent line intensities, but no other adjustments have been made to account for the instrumental response, or for the variety of plasma temperatures and densities represented in the data. Portions of the spectrum below ~7.4 Å and above ~8.8 Å are of lower quality because of unavoidable instrumental effects. Small gaps in the data (with labels in parentheses) are where non-Fe emission lines have been excluded for clarity. The labeling convention for Fe and Cr lines is as follows: L for Li-like Fe XXIV, E for Be-like Fe XXIII, B for B-like Fe XXII, and C for C-like Fe XXI; Cr for Cr XXII; U for unidentified.

Model spectra are shown both with and without wavelength adjustments. For the adjusted spectrum, 0.7 eV was added to each C-like line, 1.2 eV to each B-like line, and 1.9 eV to the six Be-like transitions having lower level $2s2p\,^1P_1$ (lines E11, E10, E5, E4, E2, and part of E1). As explained in the text, these few systematic corrections bring virtually all model lines into excellent agreement with observed wavelengths. Calibration lines from Na and Mg are shown across the top.

lengths are systematically about 6 or 7 mÅ longer than the measured values; if 1.2 eV is added to the theoretical energies of all Fe XXII lines listed in Table 3, then the maximum difference between calculated and measured wavelengths is only 0.001 Å (excluding the three tentatively identified B-like lines that will be discussed in § 4.3). The theoretical wavelengths for the C-like lines are all approximately 0.004 Å longer than those experimentally measured (equivalent to a difference of 0.6 eV), except for line C4, which has a calculated wavelength 0.007 Å shorter than that observed.

On theoretical grounds we expect HULLAC predictions to be more reliable than previous predictions, since the HULLAC models include more energy levels ($n_{max} = 6$ or 7) and predict emergent line intensities rather than just oscillator strengths. Intensity predictions based solely on oscillator strengths can be misleading when levels are populated by mechanisms other than direct dipole electron impact excitation, or when they decay via forbidden transitions or multiple branches. A good example is provided by the Fe XXIV $4 \rightarrow 2$ lines. Although the radiative rates (and thus

oscillator strengths) for $2s$–$4d$ ($\Delta L = 2$) transitions are negligibly small, the $4d$ levels are populated from the $2s$ level by nondipole collisional excitation and then decay via fully allowed transitions to produce $4d \rightarrow 2p$ lines (L9 and L7) that are just as strong as the $4p \rightarrow 2s$ lines (L5 and L6).

Our expectations are met by the excellent agreement between measurements and theory with regard to wavelengths (after the few systematic adjustments described above) and relative line intensities within each ion species. This gives us confidence in our line identifications even when they may disagree with previous work. In the following subsections we discuss the results in more detail, beginning with emission from different ion stages of Fe, followed by unidentified Fe lines, and concluding with emission from elements other than Fe.

4.1. Lithium-like Fe XXIV

Fe XXIV has 10 significant emission lines between 7.1 and 9 Å, of which we are able to observe the eight that lie above 7.4 Å. Agreement between observation and theory is ex-

TABLE 3
IRON SPECTRAL LINES

Line Identification[a]	λ_{obs} (Å)[b]	λ_{calc} (Å)	Fe Ion	Transition
L1	7.169[c]	7.1649[d,e] 7.1692[d,e]	XXIV	$2s\ ^2S_{1/2}$–$5p\ ^2P_{3/2,1/2}$ (weighted average = 7.1664 Å)
L2	7.370[c]	7.368[d] 7.3670[e]	XXIV	$2p\ ^2P_{1/2}$–$5d\ ^2D_{3/2}$
L3	7.437[d] 7.438[c]	7.437[d] 7.4363[e]	XXIV	$2p\ ^2P_{3/2}$–$5d\ ^2D_{5/2}$
L4[f]	7.457[d]	7.461[d] 7.4601[e]	XXIV	Tentative identification: $2p\ ^2P_{3/2}$–$5s\ ^2S_{1/2}$
E1[g]	~7.478[d] 7.472[c]	7.473[d] (7.489)[d] 7.475[h]	XXIII (XXIII)	$2s^2\ ^1S_0$–$2s5p\ ^1P_1$ (28% from $2s2p\ ^1P_1$–$2s6d\ ^1D_2$)
E2[f]	7.498[d]	7.506[d]	XXIII	$2s2p\ ^1P_1$–$2s6s\ ^1S_0$
B1[g]	7.6812 (4)[d] 7.680[c] 7.682[i]	7.687[d] (7.683)[d] (7.680)[h]	XXII (XXIII) (XXIII)	$2s^22p\ ^2P_{1/2}$–$2s^26d\ ^2D_{3/2}$ (dominates previously identified line $2s2p\ ^3P_1$–$2s5d\ ^3D_2$ in Fe XXIII[h])
E3	7.733[d] 7.733[c]	7.736[d] 7.734[h]	XXIII	$2s2p\ ^3P_2$–$2s5d\ ^3D_3$
B2[f]	7.752[d]	7.757[d]	XXII	$2s^22p\ ^2P_{3/2}$–$2s^26d\ ^2D_{5/2,3/2}$
B3[f]	7.865[d]	7.870[d]	XXII	$2s^22p\ ^2P_{1/2}$–$2s2p_{1/2}\ 5p_{1/2,3/2}(J = 1/2, 3/2)$
E4[f]	7.9009 (5)[d] 7.902[j] 7.901[c]	7.911[d] 7.886[h]	XXIII	$2s2p\ ^1P_1$–$2s5d\ ^1D_2$
E5[f]	7.936[d]	7.947[d]	XXIII	$2s2p\ ^1P_1$–$2s5s\ ^1S_0$
L5	7.9857 (2)[d] 7.986[j] 7.986[i] 7.984[k] 7.983[c]	7.986[d] 7.9862[e] 7.985[j] 7.986[l] 7.979[m]	XXIV	$2s\ ^2S_{1/2}$–$4p\ ^2P_{3/2}$
L6	7.9960 (4)[d] 7.996[j] 7.996[i] 7.992[k] 7.993[c]	7.996[d] 7.9964[e] 7.995[j] 7.996[l] 7.989[m]	XXIV	$2s\ ^2S_{1/2}$–$4p\ ^2P_{1/2}$
B4	8.0904 (3)[d] 8.091[j]	8.097[d] 8.074[j]	XXII	$2s^22p\ ^2P_{1/2}$–$2s^25d\ ^2D_{3/2}$
C1[f]	8.1536 (5)[d] 8.153[i]	8.157[d]	XXI	$2s^22p_{1/2}\ 2p_{1/2}\ (J = 0)$–$2s^22p_{1/2}\ 6d_{3/2}\ (J = 1)$
B5[f]	8.1684 (4)[d] 8.167[c]	8.174[d]	XXII	$2s^22p\ ^2P_{3/2}$–$2s^25d\ ^2D_{5/2,3/2}$
C2[f]	8.2036 (9)[d]	8.206[d]	XXI	$2s^22p_{1/2}\ 2p_{3/2}\ (J = 1)$–$2s^22p_{1/2}\ 6d_{5/2}\ (J = 2)$
L7	8.2326 (4)[d] 8.232[j] 8.233[i] 8.231[k] 8.231[c]	8.234[d] 8.232[j] 8.2322[e] 8.232[l] 8.225[m]	XXIV	$2p\ ^2P_{1/2}$–$4d\ ^2D_{3/2}$
B6[f]	8.274[d] 8.273[c] 8.271[k]	8.283[d]	XXII	Tentative identification: $2s2p_{3/2}\ 2p_{3/2}\ (J = 5/2)$–$2s2p_{3/2}\ 5d_{1/2}\ (J = 7/2)$; previous identification[h]: Fe XXIII $2s2p\ ^3P_2$–$2p4p\ ^3D_3$
L8	8.2850 (4)[d] 8.2854 (7)[n] 8.285[c] 8.289[k]	8.287[d] 8.2862[e] 8.279[m] 8.284[l]	XXIV	$2p\ ^2P_{1/2}$–$4s\ ^2S_{1/2}$
E6	8.3038 (3)[d] 8.3040 (7)[n] 8.305[j] 8.305[i] 8.303[k] 8.303[c]	8.304[d] 8.305[j] 8.306[h] 8.306[m]	XXIII	$2s^2\ ^1S_0$–$2s4p\ ^1P_1$
L9	8.3161 (3)[d] 8.3160 (7)[n] 8.317[j] 8.318[i] 8.316[k] 8.316[c]	8.319[d] 8.3171[e] 8.317[j] 8.317[l] 8.311[m]	XXIV	$2p\ ^2P_{3/2}$–$4d\ ^2D_{5/2,3/2}$; also Fe XXIII $2s2s\ ^1S_0$–$2s4p\ ^3P_1$, at $\lambda_{calc} = 8.317$;[d,j] the shoulder on the long side is $5 \rightarrow 2$ transitions in Fe XXII and Fe XXI

TABLE 3—*Continued*

Line Identification[a]	λ_{obs} (Å)[b]	λ_{calc} (Å)	Fe Ion	Transition
L10	8.3761 (7)[d] 8.3757 (7)[n] 8.376[i] 8.371[c]	8.376[d] 8.3758[e] 8.373[l] 8.368[m]	XXIV	$2p\,^2P_{3/2}$–$4s\,^2S_{1/2}$; also about 15% from Fe XXII $2s2p_{1/2}\,2p_{3/2}$ ($J = 3/2$)–$2s2p_{1/2}\,5s(J = 1/2)$ at $\lambda_{calc} = 8.387$;[d] the shoulder on the short side is a $6 \to 2$ Cr XXII line
B7[f]	8.4053 (6)[d] 8.4055 (7)[n] 8.406[c]	8.421[d]	XXII	Tentative identification: $2s2p_{1/2}\,2p_{3/2}$ ($J = 1/2$)–$2s2p_{1/2}\,5d_{5/2}$ ($J = 3/2$); observed intensity is about twice that predicted
E7	8.529[d] 8.528[k] 8.529[c]	8.529[d] 8.527[h]	XXIII	$2s2p\,^3P_0$–$2s4d\,^3D_1$
E8[g]	8.546[d] 8.550[j] 8.547[k] 8.550[c]	8.551[d] (8.547[d]) 8.552[j] 8.548[h]	XXIII (XXI)	$2s2p\,^3P_1$–$2s4d\,^3D_{2,1}$ [and $2s^22p_{1/2}\,2p_{3/2}$ ($J = 1$)–$2s^2\,2p_{3/2}\,5d_{3/2}$ ($J = 2, 1, 0$)]
C3[g]	8.5740 (8)[d] 8.573[j] 8.574[i] 8.575[c]	8.578[d] (8.581)[d] 8.573[j]	XXI (XXI)	$2s^22p_{1/2}\,2p_{1/2}$ ($J = 0$) $^3P_0$–$2s^22p_{1/2}\,5d_{3/2}$ ($J = 1$) $^3D_1$ [and $2s^22p_{1/2}\,2p_{3/2}$ ($J = 2$)–$2s^22p_{3/2}\,5d_{3/2}$ ($J = 3$)]
E9	8.6172 (6)[d] 8.616[j] 8.619[i] 8.614[k] 8.614[c]	8.617[d] 8.618[j] 8.615[h]	XXIII	$2s2p\,^3P_2$–$2s4d\,^3D_3$
C4	8.640[d] 8.644[j] 8.643[c]	8.633[d]	XXI	$2s^22p_{1/2}\,2p_{3/2}$ ($J = 1$)–$2s^22p_{1/2}\,5d_{5/2}$ ($J = 2$)
C5[f]	8.663[d] 8.660[j] 8.664[c]	8.668[d]	XXI	$2s^22p_{1/2}\,2p_{3/2}$ ($J = 2$)–$2s^22p_{1/2}\,5d_{5/2}$ ($J = 3$), $2s^22p_{3/2}\,2p_{3/2}$ ($J = 2$)–$2s^22p_{3/2}\,5d_{5/2}$ ($J = 3$)
B8	8.714[d] 8.715[j] 8.714[c]	8.720[d] 8.713[j]	XXII	$2s^22p_{1/2}\,^2P_{1/2}$–$2s2p_{1/2}\,4p_{3/2}$ ($J = 3/2$)
B9	8.720[d] 8.722[j] 8.723[c]	8.728[d] 8.723[j]	XXII	$2s^22p_{1/2}\,^2P_{1/2}$–$2s2p_{1/2}\,4p_{3/2}$ ($J = 1/2$)
B10[f]	8.736[d] 8.734[j] 8.736[c]	8.744[d]	XXII	$2s^22p_{1/2}\,^2P_{1/2}$–$2s2p_{1/2}\,4p_{1/2}$ ($J = 3/2$)
B11[f]	8.753[d] 8.752[k] 8.752[c]	8.769[d]	XXII	Tentative identification: $2s^22p_{1/2}\,^2P_{1/2}$–$2s2p_{1/2}\,4p_{1/2}$ ($J = 1/2$); observed intensity is about twice that predicted; previous identification:[h] Fe XXIII $2p^2\,^1D_2$–$2p4d\,^1F_3$ but very weak at normal densities, and $\lambda_{calc} = 8.737$[d]
E10	8.8149 (4)[d] 8.815[j] 8.811[i] 8.812[k] 8.814[c]	8.826[d] 8.826[j] 8.794[h]	XXIII	$2s2p\,^1P_1$–$2s4d\,^1D_2$
E11	8.906[d] 8.906[j] 8.906[k] 8.908[c]	8.918[d] 8.919[j]	XXIII	$2s2p\,^1P_1$–$2s4s\,^1S_0$
B12	8.9748 (6)[d] 8.976[j] 8.975[i] 8.977[c]	8.982[d] 8.976[j] 8.952[h]	XXII	$2s^22p\,^2P_{1/2}$–$2s^24d\,^2D_{3/2}$

[a] Labeling convention: L for Li-like Fe XXIV, E for Be-like Fe XXIII, B for B-like Fe XXII, C for C-like Fe XXI, U for unidentified.
[b] Numbers in parentheses give the uncertainty of the measured wavelength in tenths of 1 mÅ. When no error is listed, the uncertainty is 1 or 2 mÅ.
[c] Laser plasma observations by Boiko et al. 1978.
[d] This work.
[e] Theoretical calculations by Vainshtein & Safronova 1985.
[f] New identification.
[g] Clarification of previously published identification.
[h] Theoretical calculations by Bromage et al. 1978.
[i] Solar observations (with wavelength corrections) by McKenzie et al. 1985.
[j] Solar observations and theoretical calculations by Fawcett et al. 1987.
[k] Laser plasma observations by Fawcett & Ridgeley 1979.
[l] Theoretical calculations by Edlen 1979.
[m] Theoretical calculations by Doschek et al. 1972.
[n] Solar observations by Seely & Feldman 1986.

cellent, except for the wavelength and intensity of L4 ($2p\,^2P_{3/2}$–$5s\,^2S_{1/2}$). The measured wavelength of L4 is at least 0.003 Å lower than predicted, and its observed intensity is roughly 3 times higher than predicted. It is possible that the "true" $2p\,^2P_{3/2}$–$5s\,^2S_{1/2}$ transition is obscured by the wing of Mg Kγ, and that line L4 is in fact some other, unknown transition, but we are unable to suggest any likely candidates. We therefore label our identification of L4 as tentative.

4.2. *Beryllium-like* Fe XXIII

Of the 11 Fe XXIII transitions listed, four are new. They are the $6 \rightarrow 2$ and $5 \rightarrow 2$ analogs of the previously identified $4 \rightarrow 2$ transitions $2s2p\,^1P_1$–$2s4d\,^1D_2$ (E10 at 8.815 Å) and $2s2p\,^1P_1$–$2s4s\,^1S_0$ (E11 at 8.906), and correspond to, respectively, line E1 at ~ 7.478 Å (in which the $2s2p\,^1P_1$–$2s6d\,^1D_2$ transition has about one-third of the intensity of the previously identified $2s^2\,^1S_0$–$2s5p\,^1P_1$ transition); E2 at 7.498 Å; E4 at 7.901 Å (which had been incorrectly assigned to a line at 7.883 Å by Bromage et al. 1978 in their study of the Boiko et al. 1978 laser plasma spectra); and E5 at 7.936 Å.

The wavelength of the E1 blend is not well measured in our data, but when the 1.9 eV correction (see § 4) is applied to the $2s2p\,^1P_1$–$2s6d\,^1D_2$ component, we predict a centroid of 7.474 Å for the blend. It was found that the E8 line is also a blend, consisting of a Be-like line and a cluster of $5 \rightarrow 2$ transitions in C-like Fe.

4.3. *Boron-like* Fe XXII

There are several new or reidentifications of Fe XXII lines, including a few density-sensitive lines whose use as diagnostics will be discussed in § 5. Lines B1 and B2 are $6 \rightarrow 2$ transitions, which are quite strong in some of our spectra. The B1 transition $2s^22p\,^2P_{1/2}$–$2s^26d\,^2D_{3/2}$ was found to dominate a previously identified but much weaker transition in Fe XXIII. Nearly as strong as B1 are lines B2 and B3

(a newly identified $5 \rightarrow 2$ transition), but their wavelengths could not be measured as precisely because they were partially obscured by the so-called w and z lines of He-like Al XII (see Table 5).

The identification of B5 (along with the C-like line, C1) solves a puzzle in a series of solar flare spectra reported 25 years ago by Doschek et al. (1972). They observed six strong lines or blends between 7.95 and 8.40 Å and were able to correctly identify four as transitions in Fe XXIV and XXIII, leaving two unknown features around 8.10 and 8.16 Å. They correctly suggested that the first line (which we label B4) might be the $2s^22p\,^2P_{1/2}$–$2s^25d\,^2D_{3/2}$ transition in Fe XXII but were puzzled by the second "doublet" feature, which did not weaken over time (as the flare cooled and the ions recombined) like any of the other lines. That second feature is the blend of C1 and B5 (8.154 and 8.168 Å, respectively). As the flare cooled and B-like emission decreased, the net intensity of the C1/B5 blend was maintained by emission from the increasing population of C-like ions. The B5 line itself consists of two transitions, one of which is sensitive to density.

The only other new Fe XXII identification that we consider firm is the B10 line at 8.736 Å, but we have also made three other tentative line identifications: B6 at 8.274 Å, B7 at 8.4053 Å, and B11 at 8.753 Å. All of these features have been observed in laser plasma spectra, and B7 has also been seen quite distinctly in a solar spectrum by Seely & Feldman (1986). Our model calculations showed that earlier identifications of B6 and B11 by Bromage et al. (1978) were incorrect; the intensities of their proposed lines are negligible at astrophysical (coronal) densities, and the expected wavelength of their proposed B11 transition is off by at least 0.015 Å. Our own identifications of these three lines, however, also must be treated with caution because of disagreements between observation and calculation that are

TABLE 4

UNIDENTIFIED IRON LINES

Line Identification[a]	λ_{obs} (Å)[b]	Comments
None	7.919[c]	Weak, probably Fe XXI $2s^22p_{1/2}2p_{3/2}$ ($J = 1$)–$2s2p_{1/2}2p_{3/2}6p_{3/2}$ ($J = 2, 1$) at $\lambda_{\mathrm{calc}} = 7.924$;[d] we observe a weak feature at 7.919 Å
None	7.949[e]	We observe a weak feature at ~ 7.950 Å
None	8.141[e]	We observe a weak feature at 8.138 Å
None	8.2557 (7)[f]	
U1	8.560[d]	
U2	8.919[d] 8.918[c] 8.920[e] 8.921[g]	Always present, but usually weak in our data; intensity may scale with that of U3
U3	8.937[d]	Probably from the same ion as U2
U4	~ 9.009[d] 9.006[c] 9.006[g]	Previous identification:[h] Fe XXII $2s2p^2\,^4P_{5/2}$–$2s2p4d\,(^3P)^4D_{7/2}$, but very weak at normal densities

[a] Labeling convention: L for Li-like Fe XXIV, E for Be-like Fe XXIII, B for B-like Fe XXII, C for C-like Fe XXI, U for unidentified.

[b] Numbers in parentheses give the uncertainty of the measured wavelength in tenths of 1 mÅ. When no error is listed, the uncertainty is 1 or 2 mÅ.

[c] Solar observations and theoretical calculations by Fawcett et al. 1987.

[d] This work.

[e] Solar observations (with wavelength corrections) by McKenzie et al. 1985.

[f] Solar observations by Seely & Feldman 1986.

[g] Laser plasma observations by Boiko et al. 1978.

[h] Theoretical calculations by Bromage et al. 1978.

TABLE 5

NON-IRON EMISSION LINES

Line Identification	Ion	λ_{obs} (Å)	λ_{ref} (Å)	Transition
Se1	Se^{24+}	7.6907 (3)	7.685[a]	$2s^2 2p^6\,{}^1S_0 - 2s^2 2p^5 3d\,{}^1P_1$
Al w	Al^{11+}	7.7573 (2)	7.7573[b]	$1s^2\,{}^1S_0 - 1s2p\,{}^1P_1$
Al xy	Al^{11+}	7.8067 (5)	7.8065[b,c]	$1s^2\,{}^1S_0 - 1s2p\,{}^3P_{2,1}$
Mg Kβ	Mg^{10+}	7.8503 (2)[d]	7.8507[e]	$1s^2\,{}^1S_0 - 1s3p\,{}^1P_1$
Al z	Al^{11+}	7.8722 (3)	7.8721[b]	$1s^2\,{}^1S_0 - 1s2s\,{}^3S_1$
Se2	Se^{24+}	7.8779 (3)	7.874[a]	$2s^2 2p^6\,{}^1S_0 - 2s^2 2p^5 3d\,{}^3D_1$
Se3	Se^{23+}	7.9667 (7)		
Se4	Se^{23+}	7.9744 (6)		
Cr1	Cr^{21+}	8.519	8.516[f,g]	$2s\,{}^2S_{1/2} - 5p\,{}^2P_{3/2,1/2}$
Cr2	Cr^{21+}	8.777	8.7749[g]	$2p\,{}^2P_{1/2} - 5d\,{}^2D_{3/2}$
Cr3	Cr^{21+}	8.8444 (6)	8.8442[g]	$2p\,{}^2P_{3/2} - 5d\,{}^2D_{5/2}$

[a] Measured wavelength from Boiko et al. 1978.
[b] Theoretical wavelength from Drake 1988.
[c] Weighted average of 15% 7.8038 Å and 85% 7.8070 Å; weights derived from relative upper level populations of 5 : 3, and branching ratios of 0.107 and 1.0.
[d] Measured line includes small but significant contributions from $1s3l$ levels other than $1s3p\,{}^1P_1$, which slightly shift the centroid of the line.
[e] Theoretical wavelength from U. I. Safronova 1986, private communication.
[f] Weighted average of 67% 8.5140 Å and 33% 8.5183 Å.
[g] Theoretical wavelength from Vainshtein & Safronova 1985.

significantly larger than for any of the other lines we have identified. Specifically, for these lines, $\lambda_{\mathrm{calc}} - \lambda_{\mathrm{obs}}$ ranges between 0.003 and 0.009 Å (after applying the systematic 1.2 eV B-like–line energy correction), and $I_{\mathrm{calc}}/I_{\mathrm{obs}}$ varies between $\frac{1}{2}$ and $\frac{1}{3}$.

There is one other B-like worth mentioning, even though we cannot resolve it on our spectrum. Lying within the B-like emission cluster between 8.70 and 8.76 Å is a density-sensitive transition, $2s^2 2p_{3/2}\,{}^2P_{3/2} - 2s2p_{3/2}\,4p_{3/2}$ ($J = 5/2$), which we predict lies at 8.730 Å (following the 1.2 eV correction). Although relatively weak in our spectrum, the relative intensity of this transition is predicted to increase by a factor of more than 5 between 10^{13} and 10^{14} cm^{-3} so that it becomes stronger than the B10 line, but because of blending with nearby lines, it is somewhat difficult to use it as a density diagnostic. Fortunately, there is a pair of B-like lines around 9.0 Å that are very strong, well separated from other lines, and whose intensity ratio is a function of density (see § 5).

4.4. Carbon-like Fe XXI

All five of the C-like features that we identify in Table 3 have been observed in solar spectra, including the relatively weak C2 line, which can be discerned in the spectra of Doschek et al. 1972. Only one of those lines, however, has been previously (partially) identified: the C3 line at 8.574 Å.

At low densities, C3 is the brightest of all the C-like $5 \rightarrow 2$ features. This line is actually a blend of four transitions, although at densities below 10^{14} cm^{-3} the density-insensitive transition originally identified by Fawcett et al. (1987) is strongest. The other three transitions are $2s^2 2p_{1/2}\,2p_{3/2}$ ($J = 2$) $- 2s^2 2p_{3/2}\,5d_{3/2}$ ($J = 3$), $2s^2 2p_{1/2}\,2p_{3/2}$ ($J = 2$) $- 2s^2 2p_{3/2}\,5d_{5/2}$ ($J = 2$), and $2s^2 2p_{1/2}\,2P_{3/2}$ ($J = 2$) $- 2s^2 2p_{3/2}\,5d_{3/2}$ ($J = 1$), with relative strengths of approximately $7 : 3 : 1$. Between 10^{11} and 10^{13} cm^{-3} their intensity increases almost 6 times faster than density, and their combined strength equals that of the density-insensitive transition at around 3×10^{13} cm^{-3}. Like C3, the C4 and C5 lines (C5 is a blend with two dominant transitions) are also

density sensitive, and surpass C3 in intensity above approximately 10^{14} cm^{-3}. These and other potential diagnostic lines are discussed further in § 5.1.

4.5. Unidentified Lines

We are unable to identify a number of lines we observed. Those lines, and any other unclassified lines previously seen in solar spectra between 7.0 and 9.1 Å, are listed in Table 4. The line at 7.871 Å seen by Fawcett et al. (1987) in a solar flare spectrum is undoubtedly from Al XII $1s^2\,{}^1S_0 - 1s2s\,{}^3S_1$, and is not listed. Although there are some features in the model spectrum near U2, U3, and U4, they are much too small compared to the predicted intensities of E10 and B12 to explain the relative intensities of the observed lines. (Recall that lines near the edge of the spectrum are suppressed by instrumental effects.)

In our efforts to identify the lines in question, satellite lines of iron and emission from C-, N-, and O-like nickel were investigated using HULLAC, but no plausible candidates were found. Although deficiencies in the atomic models, exotic plasma processes in the tokamak or solar corona, emission from trace elements, and similar explanations cannot be entirely excluded, we suggest that most of the unclassified lines likely come from lower ionization stages of iron such as N-like Fe XX and O-like Fe XIX. Because of the complexity in modeling those ions, particularly with the high-n atomic levels that would be required ($n \geq 5$), and because of uncertainties in the relative intensities of the unidentified lines near the edge of the spectrum, we have not pursued those investigations further.

4.6. Non-Fe Emission Lines

In addition to emission from Fe ions (and the calibration lines from Na and Mg), we also observed lines from three other elements that were present in the tokamak as impurities: Al, Se, and Cr. The aluminum is from the housing of a probe used to make plasma-edge measurements. The selenium was left over from injection during a preceding experiment and appeared only in the early stages of our experiment. Chromium, like iron, is a component of the

stainless-steel containment vessel and is always present, although at only about 10% the level of iron. Nickel is also present for the same reason, but as described above, was not observed. The remaining few percent of the stainless steel chamber consists mostly of manganese, which has negligible emission at such a low concentration.

Ten emission lines from the above three elements are listed in Table 5, along with Mg Kβ, a calibration line that was itself calibrated using Na Lyman lines as discussed in § 2.3. The Al lines are He-like Kα transitions, specifically the resonance line $(1s^2\ ^1S_0-1s2p\ ^1P_1)$, intercombination line blend $(1s^2\ ^1S_0-1s2p\ ^3P_{2,1}$ with 85% from $^3P_1)$, and forbidden line $(1s^2\ ^1S_0-1s2s\ ^3S_1)$. We believe that our wavelength measurements of these lines known respectively as w, x, y, and z in the notation of Gabriel (1972) are the most accurate to date, and note that they are essentially in perfect agreement with the predictions of Drake (1988).

Se1 and Se2, the two most prominent selenium lines we observe, are from transitions in Ne-like Se xxv. These lines are quite strong in one of our shots, allowing us to determine their wavelengths with an uncertainty of only 0.0003 Å. The wavelengths we measure are about 0.004 Å longer than those measured by Boiko et al. (1978). Based on previous work (Beiersdorfer et al. 1989), we also identified Se3 and Se4 as transitions in Na-like Se xxiv.

As discussed before, our theoretical model includes Li-like Cr xxii and Be-like Cr xxi. Emission from chromium is generally weak, but we are able to confidently identify three lines as $5 \rightarrow 2$ transitions in Cr xxii. There are some indications of $6 \rightarrow 2$ and $7 \rightarrow 2$ emissions at 8.365, 8.099, 8.065, and 8.041 Å, but these features are weak and are not listed in the table. No emission from Cr xxi is observed.

5. DENSITY DIAGNOSTICS

The density sensitivities of Fe xxi and Fe xxii spectra have been discussed by Doschek et al. (1973) for the $3 \rightarrow 2$ transitions, Mason & Storey (1980), who include calculations of the $4 \rightarrow 2$ lines, and Fawcett et al. (1987), who treat the $4 \rightarrow 2$ spectrum from an experimental point of view. In general, the density sensitivity of Fe L-shell spectra derives from the buildup of population in low-lying metastable states at densities exceeding $\sim 10^{12}$ cm^{-3}. Each of those low-energy excited levels can then serve as a platform for excitation to higher energy levels via electron collisions, often producing a set of lines that is distinct from that observed at low densities, and whose intensity varies more rapidly with electron density than lines produced by excitation from the ground state.

At low densities ($< \sim 10^{11}$ cm^{-3}), C-like Fe xxi lines are excited from the $2s^2 2p^2_{1/2}$ $(J = 0)$ ground state, but at high densities the upper levels of the C4 and C5 transitions are populated primarily by collisions from the $2p_{1/2}2p_{3/2}$ $(J = 1)$ and $2p_{1/2}2p_{3/2}$ $(J = 2)$ levels, respectively; the upper levels of the three density-sensitive transitions included in the C3 blend are populated by collisions from both of these metastable levels. While the C3, C4, and C5 lines may be useful as diagnostics, a more detailed explanation is beyond the scope of this paper, and we will concentrate instead on B-like line diagnostics.

An illustration of the density sensitivity of B-like Fe xxii spectra is shown in Figure 3, which presents model results for $4 \rightarrow 2$, $5 \rightarrow 2$, and $6 \rightarrow 2$ transitions. The two most prominent features are the line at 8.975 Å and a blend of

two lines at 9.067 and 9.070 Å. (Wavelengths were derived by adding the usual 1.2 eV B-like–ion correction to our HULLAC-calculated energies. The measured and calculated wavelengths of the 8.975 Å B12 line are in excellent agreement, and although we cannot measure the wavelengths of the other two lines because they lie just longward of our spectrometer limit, we expect their theoretical wavelengths to be accurate to within 0.001 Å.)

A schematic of the mechanism responsible for the behavior of those $4 \rightarrow 2$ lines is shown in Figure 4. A key feature is that the first excited state $2s^2 2p_{3/2}$ can decay only by a slow $M1$ transition to the ground state. Below 10^{12} cm^{-3}, collisional excitation rates are sufficiently low so that the decay is still fast enough to prevent any significant population buildup in the metastable level, while at high densities the ratio of $2p_{3/2}$ and $2p_{1/2}$ populations approaches its LTE value of 2. Between those two limits the $2p_{3/2}$ population, relative to the ground state population, increases from ~ 0.01 at 10^{12} cm^{-3} to ~ 1.5 at 10^{16} cm^{-3}. The second essential feature is that collisional excitation from the $2p_{1/2}$ level preferentially populates the $4d_{3/2}$ level (at 7.5 times the rate for the $4d_{5/2}$ level, at a temperature of 1 keV), while the $2p_{3/2}$ level tends to populate the $4d_{5/2}$ level (by a ratio of 5.3 to 1). The net result is that the population of the $4d_{5/2}$ level increases with density faster than that of $4d_{3/2}$, leading to an increase in the relative intensity of the 9.067-Å $4d_{5/2} \rightarrow 2p_{3/2}$ line. Virtually the same mechanism and analogous energy levels apply for $n = 3$, 5, and higher.
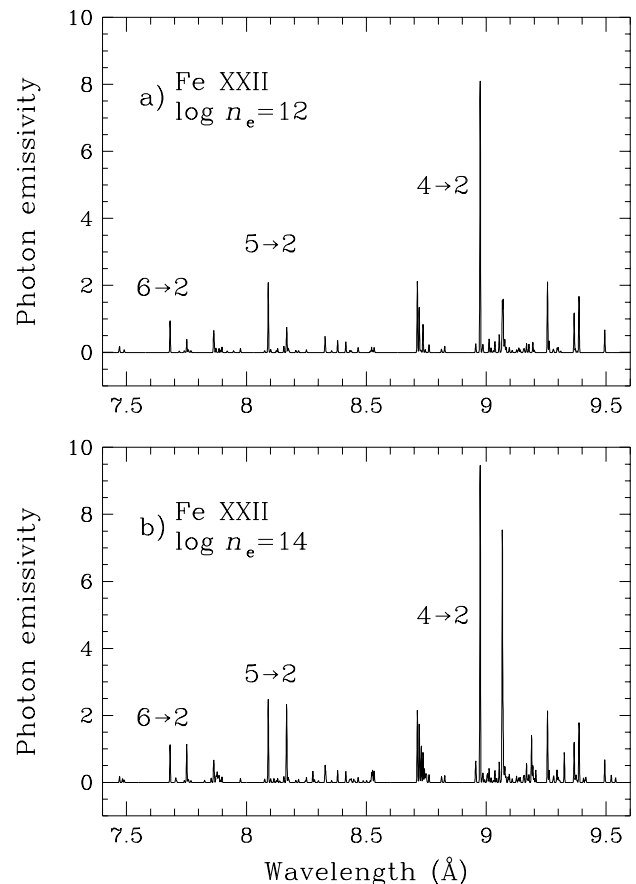

Fig. 3.—Theoretical spectra of B-like Fe xxii at electron temperature of 1000 eV, for densities of (a) 10^{12} cm^{-3} and (b) 10^{14} cm^{-3}. Emissivity units are arbitrary but the same for both panels. Spectra are plotted with a FWHM resolution of 0.003 Å.
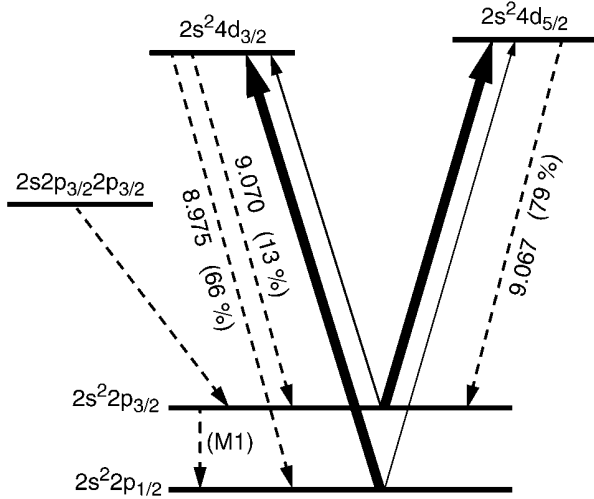
FIG. 4.—Schematic diagram of processes responsible for the density sensitivity of B-like Fe XXII $4 \rightarrow 2$ lines. Relative magnitudes of collisional-rate coefficients are represented by the thickness of the solid lines. Dotted lines indicate relevant radiative decay channels, with wavelengths (in angstroms) and radiative branching ratios (in parentheses). At low densities the dominant process is excitation of the $4d_{3/2}$ level from ground. At high densities the $4d_{5/2}$ level is excited from the metastable $2p_{3/2}$ level, which is fed by cascades mostly through the $2s2p_{3/2} 2p_{3/2}$ ($J = 1/2, 3/2, 5/2$) levels, and which decays by a slow $M1$ transition to ground.
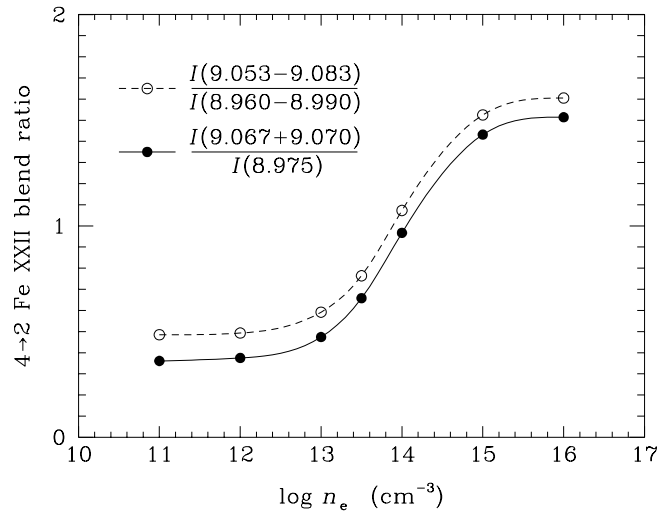

FIG. 5.—Fe XXII $4 \rightarrow 2$ line intensity ratios vs. $\log n_e$. The solid curve is the ratio of the intensities of the primary $9.067 + 9.070$ Å and 8.976 Å lines, while the dashed curve is the ratio when weak nearby lines (within 0.015 Å of the primary lines) are included. The analogous curves for the $5 \rightarrow 2$ lines (at 8.168 and 8.090 Å) are shifted upward by approximately 0.035 and 0.050, respectively.

Model predictions of the $4 \rightarrow 2$ line ratio versus density are shown in Figure 5, with the ratio rising from about 0.5 at $n_e = 10^{13}$ cm^{-3} to 1.5 at 10^{15} cm^{-3}. In addition to the plot of the ratio of the 8.975 Å and $9.067 + 9.070$ Å lines, a second curve illustrates the effect of finite spectral resolution, in which all nearby B-like lines are summed with the main peaks. In the example shown, a resolution bin of $\Delta\lambda/\lambda = 1/300$ has been used, centered on the primary lines. The difference between the two curves is small since the other B-like lines are relatively weak, but in a real spectrum the contribution of lines from other ion species must also be considered. Corresponding curves for the $5 \rightarrow 2$ lines (at 8.090 and 8.168 Å) are very similar, as one would expect, and are offset vertically from the $4 \rightarrow 2$ curves by 0.035 (for the pure lines) and 0.050 (with $\Delta\lambda/\lambda = 1/300$).

Unfortunately, the 9.067 Å line is just longward of our spectrometer limit, so we cannot apply the $4 \rightarrow 2$ diagnostic to our data. We are, however, able to use other sets of diagnostic lines—the $5 \rightarrow 2$ analogs at 8.090 (B4) and 8.168 Å (B5); the cluster of B-like lines between 8.70 and 8.77 Å (B8–B11); and the C-like C3, C4, and C5 lines between 8.6 and 8.7 Å—to deduce an electron density of 3×10^{13} cm^{-3} in the Fe XXI and XXII line-forming regions of our tokamak plasma.

We can also apply the B-like $4 \rightarrow 2$ diagnostic to the 1985 July solar flare spectrum reported by Fawcett et al. (1987). They measured a line ratio of $I(9.073)/I(8.976) = 0.54$, indicating a density of $\sim 3 \times 10^{13}$ cm^{-3}, slightly higher than their suggested value of $\sim 10^{13}$ cm^{-3}, which was derived using uncertain collision strengths and branching ratios. Features are also seen at 8.090 and 8.168 Å in that flare spectrum, but they are probably too weak to apply the $5 \rightarrow 2$ line diagnostic effectively.

6. SUMMARY

We have presented results from a study of the spectrum of highly ionized Fe between approximately 7 and 9 Å, and confirmed most previous line identifications while also cataloging over a dozen new lines, including transitions in Be-like Fe XXIII, B-like Fe XXII, and C-like Fe XXI. A method of calibrating the wavelengths of emission lines from extended sources with very high accuracy was described, and the results were compared with a comprehensive list of previous theoretical work and solar and laboratory observations. Secondary products of that calibration are what we believe to be the most accurate wavelength measurements to date of the Al Kα complex and Mg Kβ.

Theoretical spectra were calculated with the HULLAC atomic modeling package and compared with observed spectra. HULLAC employs detailed level accounting to compute emission rates, rather than relying on scaled oscillator strengths, and also uses more complete atomic models (through $n = 6$ or 7) than in previous works, so its predictions of relative line intensities should be more reliable. Agreement with observations was generally quite good with regard to both wavelengths and intensities, although a few systematic wavelength errors were seen and some lines remained unidentified.

The use of Fe L-shell line ratios as density diagnostics was examined, and a plot of B-like Fe XXII line ratios versus density provided, which we used to infer a value for electron density in a previously reported solar flare. The wavelength and intensity information presented here will provide a similar utility for the analysis of X-ray spectra from astrophysical sources once high-resolution spectra become available.

In addition to the Fe lines studied here, a number of emission lines from hydrogenic and heliumlike Na, Mg, and Al also lie in the 7–9 Å wavelength regime. Several of those lines, particularly the He-like Al XII $2 \rightarrow 1$ lines (w, x, y, and z) and He-like Mg Kβ and Mg Kγ, are useful as diagnostics but may be blended with Fe L-shell emission lines. For example, even a resolving power of 500 would be insufficient to separate the Al w-resonance line from B2, Mg Kβ

from B3, or Mg Kγ from E1 and L4. (Note that the B2 and B3 lines were not even "known" until this work.) Since Fe L-shell emission is often a prominent component of astrophysical spectra, it is vital that any plasma codes being used to analyze spectral data incorporate a sufficiently complete list of reliable line emission rates, not only to account for all the flux in the iron lines themselves, but also to give accurate diagnostic information derived from He-like lines in this region.

REFERENCES

Bar-Shalom, A., Klapisch, M., & Oreg, J. 1988, Phys. Rev. A, 38, 1773
Beiersdorfer, P., von Goeler, S., Bitter, M., & Hill, K. W. 1989, Nucl. Instrum. Methods Phys. Res., B43
Boiko, V. A., Faenov, A. Ya., & Pikuz, S. A. 1978, J. Quant. Spectrosc. Radiat. Transfer, 19, 11
Bromage, G. E., Cowan, R. D., Fawcett, B. C., & Ridgeley, A. 1978, J. Opt. Soc. Am., 68, 48
Doschek, G. A., Meekins, J. F., & Cowan, R. D. 1972, ApJ, 177, 261
———. 1973, Sol. Phys., 29, 125
Drake, G. W. F. 1988, Canadian J. Phys., 66, 586
Drake, S. A., et al. 1994, ApJ, 436, L87
Edlen, B. 1979, Phys. Scr., 19, 225
Fabian, A. C., Arnaud, K. A., Bautz, M. W., & Tawara, Y. 1994, ApJ, 436, L63
Fawcett, B. C., Jordan, C., Lemen, J. R., & Phillips, K. J. H. 1987, MNRAS, 225, 1013
Fawcett, B. C., & Ridgeley, A. 1979, MNRAS, 188, 365
Gabriel, A. H. 1972, MNRAS, 160, 99
Garcia, J. D., & Mack, J. E. 1965, J. Opt. Soc. Am., 55, 654

Hinnov, E. 1982, Nucl. Instrum. Methods Phys. Res., 202, 381
Hosea, J., Goldston, R., & Colestock, P. 1985, Nucl. Fusion, 25, 1155
Kelly, R. L. 1987, J. Phys. Chem. Ref. Data, Vol. 16, Suppl. 1
Klapisch, M., Schwab, J. L., Fraenkel, B. S., & Oreg, J. 1977, J. Opt. Soc. Am., 67, 148
Liedahl, D. A., Osterheld, A. L., & Goldstein, W. H. 1995, ApJ, 438, L115
Marmar, E. S., Cecchi, J. L., & Cohen, S. A. 1975, Rev. Sci. Instrum., 46, 1149
Mason, H. E., & Storey, P. J. 1980, MNRAS, 191, 631
McKenzie, D. L., Landecker, P. B., Feldman, U., & Doschek, G. A. 1985, ApJ, 289, 849
Peacock, N. J., Stamp, M. F., & Silver, J. D. 1984, Phys. Scr., T8, 10
Seely, J. F., & Feldman, U. 1986, Phys. Scr., 33, 110
von Goeler, S., et al. 1983, in Proc. Course on Diagnostics for Fusion Reactor Conditions, ed. P. E. Scott et al. (Brussels: Commission of the European Communities), 1, 109
Vainshtein, L. A., & Safronova, U. I. 1985, Phys. Scr., 31, 519
White, N. E., et al. 1994, PASJ, 46, L97